We are IntechOpen, the world's leading publisher of Open Access books Built by scientists, for scientists

4,800
Open access books available

122,000
International authors and editors

135M
Downloads

Our authors are among the

154
Countries delivered to

TOP 1%
most cited scientists

12.2%
Contributors from top 500 universities

WEB OF SCIENCE™

Selection of our books indexed in the Book Citation Index in Web of Science™ Core Collection (BKCI)

Interested in publishing with us?
Contact book.department@intechopen.com

Numbers displayed above are based on latest data collected.
For more information visit www.intechopen.com

10

μ-PIV for the Analysis of Flow Fields near a Propagating Air-Liquid Interface

Eiichiro Yamaguchi, Bradford J. Smith and Donald P. Gaver III
Department of Biomedical Engineering
Tulane University
USA

1. Introduction

1.1 Background

Understanding the micro-scale multi-phase fluid dynamics in the respiratory system during the airway re-opening process has been considered as one of the key aspects necessary to improve the survival rate of clinical treatments for various respiratory diseases.

In a healthy lung, the inside surface of respiratory airways is coated with a thin film of lipids and proteins called lung surfactants (LS) which dynamically alter the surface tension and stabilize airways and reduce the work of breathing. Certain clinical events, such as gastric content aspiration, pneumonia, near-drowning, toxic gas inhalation, or chest/lung trauma will trigger lung surfactant "inactivation". This inactivation is caused by the presence of LS inhibitors, including a variety of water-soluble and surface-active serum protein substances, such as albumin, fibrinogen, and IgG that are normally absent from the airway. These can leak through the capillary membrane from the damaged cells, causing LS to lose its ability to lower surface tension necessary for the lung function (Zasadzinski et al. 2010). Mechanical ventilation is inarguably a necessary life-sustaining form of medical intervention at this stage. However, since the leaked proteins inactivate the lung surfactants, the air-liquid interface exerts a wider range of excessive, irregular mechanical stresses and strains on the delicate and highly-sensitive tissues that make up the airways and alveoli of the lung, resulting ventilator-induced lung injury (VILI). This progressive failure will eventually cause more complex pathological conditions such as Acute Lung Injury (ALI) or Acute Respiratory Distress Syndrome (ARDS). Likewise surfactant deficiency, a hallmark of Respiratory Distress Syndrome of premature infants, leads to large interfacial stress that can damage airways and alveoli during an infant's first breaths which clears amniotic fluid from the airways is it introduces air to the deep lung and alveoli.

Multiple protective techniques to minimize airway epithelial damage have been developed including low-volume ventilation, positive-end-expiratory-pressure, and surfactant replacement therapy (Clements and Avery 1998). Although these techniques have contributed greatly to reducing instances of VILI, further improvements still must be made to better treat patients with fewer resulting complications (Gaver III et al. 2006). There are about 200,000 ARDS cases per year in U.S. with mortality rate of 40-46% (Mclntyre et al. 2000; Ware and Matthay 2000).

Gaver III et al. (1990; 1996) modeled the airway re-opening process by propagating a semi-infinite bubble into a narrow fluid-occluded channel with walls coated by pulmonary epithelial cells. Bilek et al. (2003) and Key et al. (2004) demonstrated using *in vitro* studies that the rate of cell damage increases with decreasing bubble propagation speed. With the aid of computational simulations, further analyses of the experimental results have indicated that the pressure gradient, not shear stress, is primarily responsible for cellular damage. The pressure gradient is the only stress component to increase with decreasing bubble velocity in the target flow conditions, indicating that excessive pressure gradients damage the cellular lining of the airway. That study has confirmed that the widely accepted stress prediction model of the collapsed airway reopening (Fig. 1) can be applied to rigid tube models.

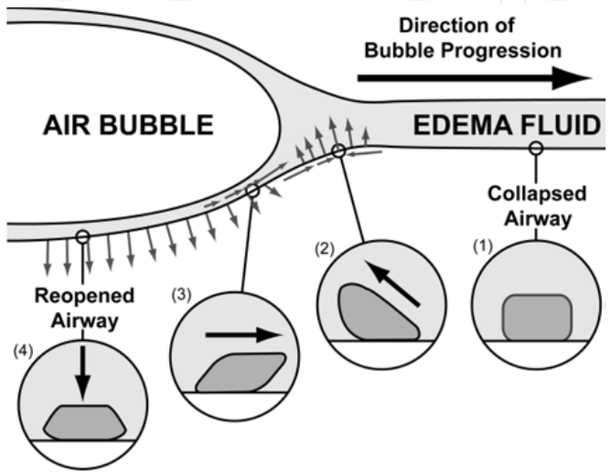

Fig. 1. Schematic of the stress distribution prediction from a model of flexible airway reopening (Gaver III et al. 1996). The cells far downstream are unstressed (1). As the bubble approaches, the cell is pulled up and toward the bubble (2). As the bubble passes, the cell is pushed away from the bubble (3). After the bubble has passed, the cell is pushed outward (4).

Follow-up studies by numerous groups have investigated this system and were found to be consistent with the theoretical predictions (Jacob and Gaver III 2005; Huh et al. 2007; Yalcin et al. 2007). Furthermore, Jacob and Gaver III (2005) included the influence of cell topography into the computational model, and found that the pressure gradient acting on the epithelial cells was even more pronounced than the original computations had demonstrated. These results have led to an interest in more detailed information of local fluid dynamics near the tip of the penetrating semi-infinite bubble. Smith & Gaver (2008) computationally investigated the flow fields surrounding a pulsating finger of air as it propagated along a rigid tube filled with a viscous Newtonian fluid. That study provides highly dynamic and intriguing spatial and temporal characteristics of the flow dynamics surrounding the bubble tip, and further elucidates the established relationship between pressure gradient and bubble velocity.

Since inactivated or insufficient amount of lung surfactants are one of important factors for controlling the cellar damage during the airway reopening, diffusive molecular transport of LS near the air-liquid interface including mechanism of competitive adsorption between lung surfactant and the inhibitors are well-studied areas (Refer to the review article of the surfactant inactivation by Zasadzinski et al. (2010) for detail.). It is predicted that for the airway reopening case, collapsing and re-spreading process of LS layer at the surface of the

progressing semi-infinite bubble tip is dominated by convective transport driven by hydrodynamics movement of the liquid phase (Fig. 2). The complex convective transport dynamics occurring during pulsatile bubble propagation are further explored using finite time Lyapunov exponents (Smith et al. 2011). During the bubble forward and retrograde bubble propagation, converging and diverging stagnation regions exist on the bubble surface due to the flow circulation in the liquid phase. It causes non-uniform non-equilibrium surfactant concentration distribution along the interface. The experimental data of pulsating bubble surfactometer (Fig. 2-i) indicates that the distribution will cause significant difference of surface tension along the interface resulting non-uniform normal stress and tangential Marangoni stress distributions across the interface. Since the shape of the bubble tip interface and thickness of liquid deposited in the wake of propagating bubble can be defined by capillary number, $Ca = \mu U / \gamma$, where μ is the dynamic viscosity of the fluid, γ is the interfacial tension, and U is the mean flow velocity (Fairbrother and Stubbs 1935), wide deviation of the interface shapes will be expected from range of surface tension during the pulsatile motions (Fig. 2-ii). The non-equilibrium stresses and interface shapes during the retracting motion will reduce both the pressure drop and deleterious mechanical stresses on the epithelial cells (Ghadialli and Gaver, 2003; Ratulowski and Chang, 1990; Yap and Gaver, 1998). Theoretical studies by Zimmer et al. (2005) suggest that pulsatile motion

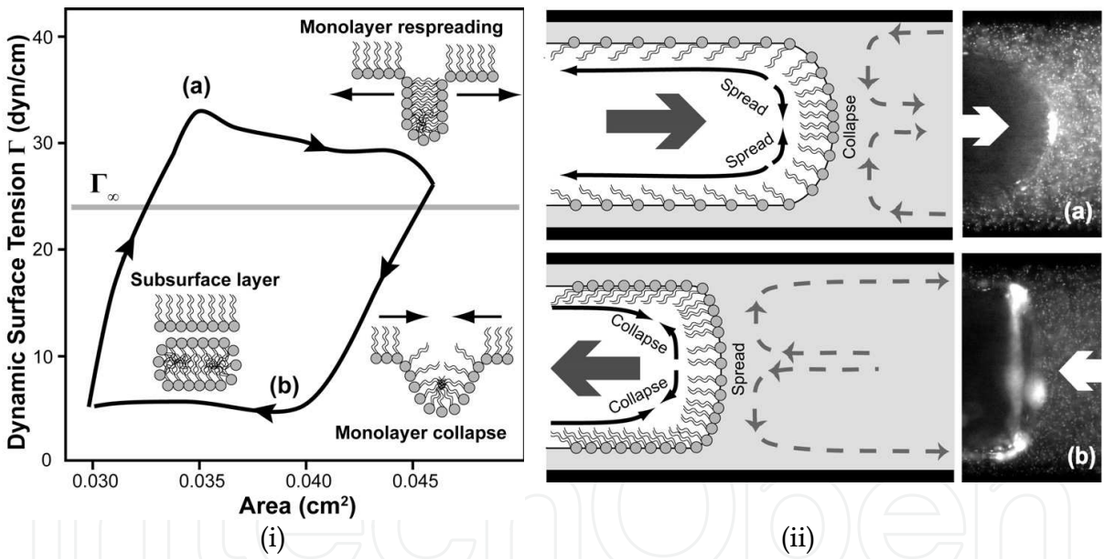

Fig. 2. (i) Hysteresis loop of dynamic surface tension from the pulsating bubble surfactometer, and graphical schemes of LS layer formation during (a) spreading and (b) collapsing of the surface (Krueger and Gaver III 2000). (ii) Prediction schemes of LS collapse and spread patterns during (a) forward progressing and (b) retracting mean motion of bubble tip. Bright spots on the fluorescent particle images on the right panels show particle flocculation indicating converging/diverging stagnation points in corresponding mean flow motions (Yamaguchi et al. 2009). The experimental observations and computer simulations indicate that pulsatile bubble motion generates a non-uniform non-equilibrium LS concentration across the interface, and the resulting Marangoni stress distribution alters the bubble interface shape accordingly.

may concentrate surfactant in high resistance regions near the progressing bubble. The bulk pressure drop measurement of a pulsating progressing bubble with LS in rigid cylindrical capillary (Pillert and Gaver III 2009) and *in-vitro* experiment of cell damage during the simulated airway reopening (Glindmeyer et al. 2011) confirmed this theory, and shown that pulsatile motion significantly reduced cell damage in comparison to linear motion airway reopening.

Due to the technical difficulties associated with whole field fluid dynamics measurements of such an unsteady interface, no experimental data are available to confirm the micro-scale relationship between the convection patterns in the sub-layer and LS distributions with local pressure and shear stress distributions. These factors also limit the investigation of LS inactivation, since identifying the difference between the inactivation and lack of LS in terms of the interface shape and the convection pattern will provide significant insight to understand the competitive adsorption mechanics.

1.2 Flow visualization of progressing semi-infinite bubble tip

Particle image velocimetry (PIV) is a well established and highly versatile technology for investigating the hydrodynamic properties of macro- and micro-scale flows (Adrian 2005). In micro-particle image velocimetry (μ-PIV) experiments, the entire test section volume is illuminated using a cone of light emanating from the recording lens, rather than the light sheet used in conventional PIV. The narrow focal depth of the objective lens results in a pseudo 2-D plane of focused particles for the correlation procedure (Santiago et al. 1998). A proper set of fluorescent seeding particles and an optical high-pass filter are employed to separate the signal from background noise. These innovations reduce the difficulties involved in creating a light sheet at the micron scale and in fabricating a microfluidic apparatus with multi-angled optical access windows that would otherwise be necessary with conventional PIV. As such, this technique is suitable to obtain instantaneous whole-field velocity information on the micro-scale.

Yamaguchi et al. (2009) performed μ-PIV investigations of flow fields surrounding a steadily progressing semi-infinite bubble tip in a smoothed wall straight glass capillary having a diameter of 312 μm. They employed a computer-controlled linear actuator system to control the steady propagation of a long finger of air, and let the bubble tip pass repeatedly under the fixed microscope observation window at controlled timing. The repeated data acquisition was necessary because the contributions of Brownian motion to an instantaneous velocity field are relatively significant and cannot be ignored due to the micron-size of the seeding particles, combined with their small displacements near the capillary tube wall. The location of the air-liquid interface in the fluorescent particle image was statistically estimated from accumulated instantaneous vector fields by identifying the significant rise of velocity fluctuations across the interface. The ensemble averaging method successfully reduced related errors for the steady low-Reynolds number flow measurements. The obtained ensemble averaged flow fields agree very well with the previously obtained computational simulations. Later the group developed a translating microscope stage system (Fig. 3) to vastly improve the capability and efficiency of image acquisition under complex flow patterns (Smith et al. 2010). The translating stage is a computer controlled sliding microscope stage that is programmed to give a counter motion opposite to the mean flow input. Therefore, in theory, the progressing bubble tip stays in the microscope

observation window regardless of the direction of bubble propagation. The combination of linear actuators and the translating stage allowed the tracking of progressing bubble tip over 10-12 cm continuously, and made it possible to obtain the flow fields under realistic airway reopening patterns, such as simulated pulsatile ventilation.

Even though it is still possible to statistically estimate the geographical location and shape of the air-liquid interface, the method does not provide sufficient accuracy to examine the bubble tip shapes under a complex flow input where the interface may experience large deformations imposed by a quick alteration of local surface tension resulted from collapsing and re-spreading of the lung surfactant on the interface. Separately obtained ensemble averaged shadowgraph images under the same flow condition could help to improve the estimation of the bubble shape deformations in relatively stable case. Smith, et al. (2011) utilize shadowgraph and μ-PIV data to examine molecular transport phenomena near the interface of the pulsating bubbles by combining the experimental data and the Finite-Time Lyapunov Exponent (FTLE), and the Boundary Element Method (BEM). They used a strobe flash lamp as the backlight illumination source, and repeat the same data acquisition process they did for μ-PIV with the addition of a custom-made microscale position indicator. Since the shadowgraph image does not contain any spatial or dynamic information to connect to corresponding PIV data, the absolute position of the bubble tip was the only information used to estimate the mean velocity input at a given instant. The different refractive index of air and liquid phases imposes a clearly visible interfacial shadow on the image. The instantaneous interfacial shapes were then averaged in discrete intervals determined by the position indicator. The ensemble-averaged bubble shapes were then superimposed on the previously obtained flow fields to give a complete description of the flow field near the interface. Although the separate shadowgraph and PIV acquisition provided satisfactory results for this simple case, the ambiguity on the estimation of mean velocity from the position indicator, difficulty of reproducing multiple identical experiments, and complex post-processing scheme will pose clear limitations for the detailed flow analysis of more unstable and realistic flow conditions.

In order to overcome these disadvantages, the simultaneous use of PIV and a pulsed shadowgraph technique to detect the precise position of air-liquid interface in slug flows for relatively large size capillaries (about 2-3 cm of diameter) was performed by Norueria et al. (2003). That group utilized a Nd:YAG laser sheet illumination technique originally used for PIV and a sheet of LED arrays for uniform backlight illumination for the pulsed shadowgraph. A single camera was used to acquire PIV and shadowgraph data simultaneously. The image was then separated during the post-processing to give an accurate instantaneous interface shape for the flow field analysis. Although it has provided sufficient accuracy and great simplicity for the relatively large scale slug flow measurement, the single camera and post–process separation are not suitable for the current microscale multiphase application. The reliability of the post process separation is limited by the low signal-to-noise (S/N) ratio at the center of the tube and near the air-liquid interface. Here, the combination of the volumetric illumination technique (μ-PIV) in conjunction with a non-uniform channel depth provides the greatest amount of noise along with strong random refraction patterns of the fluorescent emission. To compensate for this type of problem, Meinhart et al. (2000) proposed a phase-averaged velocity field algorithm to overcome these low signal-to-noise ratio situations; however, this technique is difficult to implement in a multi-phase flow scenario. Additionally, Mielink and Saetran (2006) proposed a selective

seeding method to reduce out-of-focus noise. Unfortunately, the 3-D nature of the flows investigated in our study make this technique untenable.

It is, therefore, necessary for the current application to optically separate the simultaneously acquired μ-PIV and shadowgraph images, and then record these images on two separate identical monochrome CCDs. The separation can be done by combining the proper choice of illumination sources, fluorescent materials, and epi-fluorescent filters. The images from two CCDs are then combined in post-processing to give accurate air-liquid interface information for the vector interrogation of the fluorescent images. Even though the implementation of the two cameras increases the complexity of the system development especially for optical adjustments and calibrations, it is expected to; i) be more affordable than using a three-CCD PIV capable camera, ii) have cleaner image separation by the eliminating signal interferences, and iii) have simpler post-processing.

2. Experiments

The development and descriptions of two-camera two-laser μ-PIV/Shadowgraph simultaneous data acquisition system will be described in this section. The includes the experimental setup and a brief explanation of the previously developed flow controlling system and the translating stage. Since the actual observation of the complex micro-multi-phase flows that include measurement of fluid flow fields in the neighborhood of propagating semi-infinite bubble having unsteady motions under influence of the lung surfactant can only be accomplished by combining and controlling the custom-made apparatus, the flow generating system, and the translating stage for continuous data acquisition, it is important to have dedicated subsections for each component.

2.1 Assembly of flow apparatus and the translating stage system

Continuous data acquisition of the progressing semi-infinite bubble is required for the current applications. It would not be practical to have a combination of a wide view lens with a super hi-resolution CCD in order to maintain enough spatial resolution for such a moving interface. Instead, the implementation of an interface tracking device and a moderate resolution CCD to keep the bubble tip within the fixed microscope observation window is a more practical and versatile solution to the target application. The computer-controlled translating microscope stage has been developed for this purpose. In summary, the translating stage keeps the relative position of the bubble tip within a fixed microscope observation window by mechanically sliding the entire microscope observation stage to cancel the given flow input. (a tread mill would be the closest analogy.) Precision 3-axis adjustable mechanisms for the flow apparatus allow alignment under the microscope for a flexible channel and the objective lens choices. The stage motion is controlled by attaching a computer-programmable linear actuator. A detailed technical description of this device is found in Smith et al. (2010) (Fig. 3-i provides a computer rendering of the translating stage.).

A uniform cylindrical channel with a smooth wall is the appropriate choice for the current experimental setup to the simulate airway reopening process, since most of the previous theoretical/experimental studies were associated with the similar geometrical configuration as discussed in previous section. A capillary tube made of fused silica coated with a

polyimide protective layer (Flexible Fused Silica Capillary Tubing, Polymicro Technologies, AZ) was selected because of good optical transparency and flexibility. The capillary tube was trimmed to approximately 30cm in length and the middle section (about 10 cm) of the external protective layer was carefully removed to increase the optical transparency of the observation region. It should be noted that the removal of the protecting layer will drastically decrease resistance to any kind of stress inputs, and the testing section will become extremely fragile. However, it was necessary to overcome the low transparency of the test liquid (as discussed below in the sample preparation section) in order to maintain the required fluorescent seeding density. Therefore, the removal of the protective coating would not be required for certain low seeding density applications. The capillary generally provides good transparency under Nd:YAG laser with the protective layer (Natrajan et al. 2007).

Two identical capillary tubes were closely aligned in parallel, and glued onto a 12.5x5 cm microscope slide at both ends. In order to make the capillary section straight, a custom-made holding clamp was used to provide a small amount of tension while adjusting the capillary positions on the slide glass. A custom fabricated water jacket was attached on the top of the glass slide and carefully sealed, allowing temperature control of a water reservoir at 37C during the experiments. The finished apparatus has at least 10cm of continuous observation section for two identical capillary tubes in parallel. The setting of the parallel channels was necessary to capture the bubble tip motion (the upper channel) and the stage movement (the lower quiescent channel) simultaneously (Fig. 3-iii). Even though the motion of the translating stage system is controlled by a precision linear motor, it was impossible to eliminate many sources of mechanical vibrations during the experiment. Therefore the acquisition of precise instantaneous stage movement was necessary to accurately recover actual subtracted mean velocity from the pulsatile bubble motion. To do so, the μ-PIV was used to simultaneously measure the solid body motion of a 'tracking channel' attached to the stage in order to identify the stage velocity. The 3:7 of Glycerol:Water solution with 0.02 vol% of fluorescent particles (see the sample preparation for the seeding particle choice) was mixed to achieve a neutral buoyancy, and the tracking channel was filled with the liquid and sealed on both side to prevent any external input during the experiment. The experimental channel was connected to 1/16" PEEK tubing through sets of micro-tubing attachments (Upchurch, CA) to connect the flow generating unit. Finally, the apparatus was set on the translating stage to perform continuous data acquisition of a progressing bubble over 10-12 cm of capillary under various temperatures in single experiment.

2.2 Flow generating system and the pulsatile flow input setting

An electromagnetic precision actuator system (Electromagnetic direct linear motor P01-23x80/30x90 and E200-AT, LinMot Incorporated, Switzerland) was employed to control the bubble movement. The linear motor system consists of a magnetically driven actuator with a computer-based feedback and control system. The actuator is composed of a fixed stator with a linearly-aligned electromagnet and a position sensor for feedback, paired with a magnet-filled slider. It is driven by a servo controller that is run using supplied programming and monitoring software (LinMot-Talk, LinMot Inc.). The actuator has a speed range of 1 mm/sec to 20 cm/sec with less than 0.1 % position error at a 10 cm stroke. The translating stage and appropriate sizes of micro-syringes were attached directly to the slider to provide a wide range of flexibility and control.

For the current experiment, the pulsatile flow input for simulated airway reopening is defined as the linear addition of a constant mean velocity and a sinusoidal oscillation (Fig. 3). The equation is given as

$$Ca(t) = Ca_M + Ca_\Omega \sin(\Omega t), \tag{1}$$

where Ca_M, and Ca_Ω are the mean and oscillatory capillary numbers (dimensionless velocity expression) where $Ca(t) = \mu U(t)/\gamma$, with μ is fluid viscosity, γ is the surface tension, $U(t)$ is the cross-sectional average bubble velocity, $U(t) = Q(t)/\pi R^2$, where $Q(t)$ is the time-dependent flow rate. Therefore integration over the experimental duration gives the instantaneous actuator position for the flow input of the pulsatile motion;

$$Z(t)_{total} = U_M t + A\cos(\Omega t), \tag{2}$$

where V_M is the mean velocity, and A is amplitude of the oscillation.

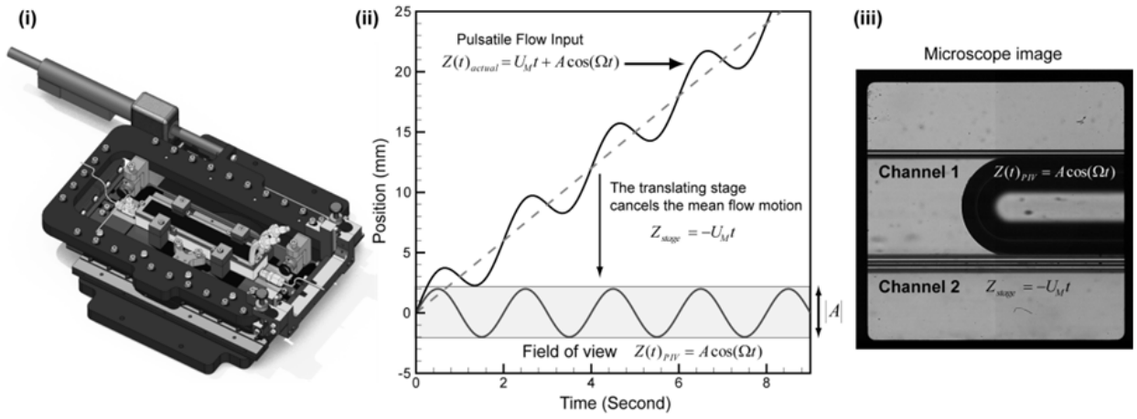

Fig. 3. (i) Scheme of the translating stage system (Smith et al. 2010), (ii) description of the flow generating system input/output, and (iii) sample microscope image of the testing section. The flow generating system is connected to channel 1, while channel 2 in Fig. 3-iii is used as the stage velocity indicator. The translating stage slides the entire microscope stage to cancel the mean bubble motion. The oscillating motion stays in the fixed microscope observation window. It significantly increases data acquisition ability and efficiency of measuring complex time dependent flows.

In order to examine the significant interfacial deformation and alterations in the flow pattern, parameters must be carefully selected to allow bubble tip retraction during the oscillation cycle without applying unrealistic frequencies and amplitudes. For the current experiment, mean bubble velocity U_M=5.5 mm/sec, amplitude A=2.0 mm, and frequency Ω=2 Hz provide a balance of the continuous acquisition efficiency over 10 seconds and the accuracy of the flow driving system. Since the target capillary tube diameter was 552 μm (see sample preparation section), a 25 μl syringe (Gastight Syringe 1707, Hamilton Company, NV) and 1 μl syringe (Microliter Syringe 7000.5, Hamilton Company, NV) were chosen to drive the mean and oscillatory component respectively. Therefore the input parameters for actuator operation were determined to be $U_{M\text{-}actuator1}$=2.97 mm/sec, $A_{actuator2}$=26.97 mm, and $\Omega_{actuator2}$ =2 Hz. The parameters fit within the range of acceptable

operational error of less than 0.1 %. The same linear actuator attached was also attached to the translating stage, and was programmed to give $U_{M\text{-}actuator3}$=-5.5 mm/sec during the data acquisition. Therefore the fixed microscope window captures the bubble tip throughout the experiment. As mentioned above, a secondary capillary was used as the instantaneous stage velocity indicator, so the recovery of absolute input velocity and cancellation of mechanical noise from the translating stage can easily be obtained from this information.

2.3 System configuration and optical setup

The μ-PIV/Shadowgraph simultaneous data acquisition system developed for the current application is depicted in Fig. 4. An inverted microscope (Nikon Eclipse TE2000-U, Nikon Corporation, Japan) with a 10x objective lens (*NA*=0.30 Plan Flour, Nikon Corporation, Japan) and two identical 2048x2048 pixel CCD cameras (12 bit, 4MP, TSI POWERVIEW Plus, TSI Incorporated, MN) provides the observation area of 1523x1523 μm with a theoretical pixel resolution of 0.744 μm/pixel. Two cameras are attached to the side optical port by using double port adapter (Y-QT, Nikon Corporation, Japan).

For the μ-PIV, the volumetric illumination was provided by a dual pulse Nd:YAG laser (λ=532 nm, Power=15mJ/pulse, Pulse duration=4 ns, New Wave Laser Pulse Solo Mini, New Wave Research, CA). The beam was directed via fiber optics to an optical port on the microscope. It was then refracted by the epi-fluorescent prism/filter cube and guided through the objective lens to volumetrically illuminate the whole test section under the field of view. The sample liquid inside of the capillary tube was seeded with d_p=1 μm fluorescent particles (refer to sample preparation section for details) that have excitation/emission peaks at 535/575 nm. Therefore only returning emission from the particles passed the dichroic filer (λ>550 nm) in the first cube. Finally, it was navigated to CCD Camera A through the second filter set (epi-fluorescent prism/filter cube 2 in Fig. 4.) to provide a pure fluorescent particle image of the test section.

For the shadowgraph, an LED pulsed red laser (λ=660 nm, Power=2nJ/pulse, Pulse duration=15ns, MPL-III-660, Opto Engine LLC, UT) was selected for source of the backlight illumination. The laser is directed via fiber optics to the top of the flow apparatus where the collimator (*NA*=0.25, *f*=36.01mm, F810FC-780, ThorLabs, NJ) is attached directly above the observation window providing approximately 1.0 cm diameter spot of uniform illumination. The projected shadowgraph image signal shares the same optical path with the μ-PIV signal. It passes the first and second dichroic filters, and was navigated to CCD Camera B to record the shadowgraph image of the air-water interface.

The epi-fluorescent prism/filter cube 2 was selected to minimize cross-talk especially on CCD Camera A due to the signal-to-noise ratio sensitivity of vector interrogation process. Since images on CCD Camera B were used only to detect the bubble interface shape, and unmistakable sharp contrast at the air-liquid interface, clarity of the shadowgraph data was often dominated by setting of the illumination strength. A dichroic prism having a combination of a low-pass filter at 625 nm (625DCLP, Chroma Technology Corp, VT) and a cleaning band pass filter of 595nm/±40nm (D595/40x, Chroma Technology Corp, VT) provided excellent separation of the fluorescent particle image for CCD Camera A.

Timing of the cameras and lasers were controlled by a multi-channel laser pulse synchronizer (Model 610035, TSI Inc.) which also sends a queue signal for the linear actuator

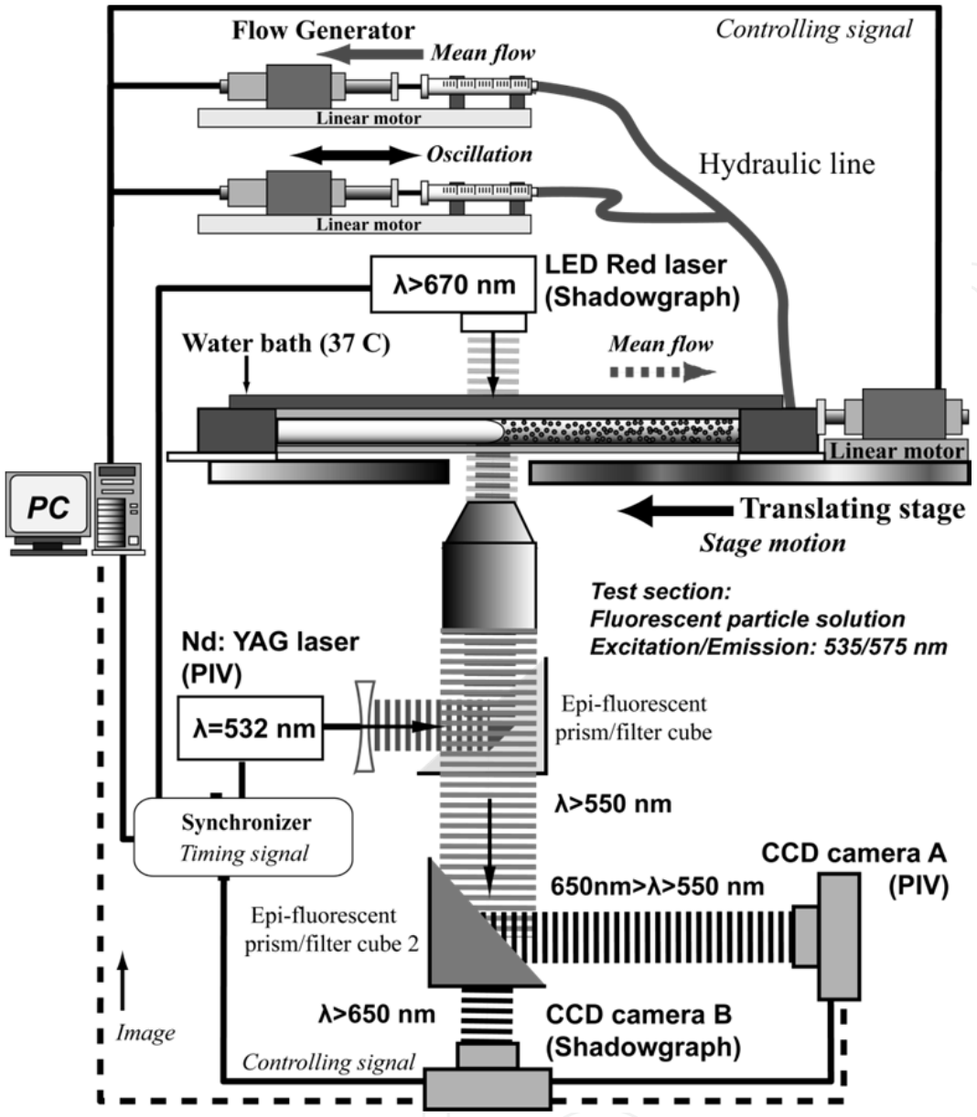

Fig. 4. Schematic of the simultaneous μ-PIV/shadowgraph data acquisition system. The system utilizes two identical monochrome cameras, two lasers having different wave length, and two dichroic beam separation filter sets to simultaneously record μ-PIV and shadowgraph images. Continuous data acquisition of the progressing bubble tip having unsteady motions is achieved by the integrated precision linear motor that generates flow and translates the microscope stage system.

flow generating system and the translating stage. Since the μ-PIV employs cross-correlation analysis, two separate fluorescence images separated by a very short time (dT=200-700 ns) were captured at every data acquisition time-point. On the other hand, the shadowgraph requires only one frame and one exposure to obtain the data at the same time-point. The timing and control signals for the cameras and lasers were, therefore, adjusted to capture one shadowgraph image at the timing of the first frame exposure of the μ-PIV. The system management, data acquisition control, and image display are controlled by Insight 3G (TSI Inc., MN).

2.4 Preparation of sample testing liquid and preliminary stability test

Nile Red was selected as fluorescent material for the current μ-PIV application due to excitation/emission peaks combination at λ=535/575 nm, since the emission spectrum was ideal for the combination with the LED red laser (λ=675 nm) for the shadowgraph. Then fluorescent particle diameter was determined as d_p=1 μm (Nile Red FluoSpheres, Invitrogen Corporation, CA) based on previously discussed pixel resolution of the observation window.

The vector interrogation window size (32x32 pixels with 50 % overlap) was determined by combination of a pixel resolution, and capillary diameter. For the current research objectives, it was preferred to have at least 40 vectors across the diameter of the capillary in order to allow detailed examination near the air-liquid interface. Since the capillary diameter D=552 μm has been set by balancing the slowest reliable velocity of the linear motors and the maximum experimental duration of the chosen syringe size, $552/(0.744*40)=18.55$ pixels/vector provide sufficient resolution. Particle seeding density was determined by trial and error using measurement of Poiseulle flow with the same capillary tube and the same pixel resolution after initial estimation of density by using the methodologies described in Olsen and Adrian (2000) and Meinhart et al. (1999). Visibility is lowest at the center of the capillary because the transparency of the liquid is limited by the concentration of lung surfactant and other proteins. Therefore, the optimal seeding concentration was determined by limiting vector loss during the interrogation at the centerline to less than 1.0 % and the axial vector fluctuation of the time ensemble averaged velocity to within 2.0 % in the $r < 0.9R$ region, where r is radial coordinate and R is radius of capillary. The seeding density 0.02 vol% with d_p=1.0 μm particle for the current setup was determined to meet there criteria.

Dulbecco's Phosphate Buffered Saline 1x (DPBS) (Invitrogen, CA) was used as a base buffer solution. This is the buffer solution adjusted to have the same osmolarity and ion concentration as that of human serum. It also contains the necessary ions, such as sodium chloride, sodium phosphate, and potassium phosphate, for the lung surfactant proteins to be functional. Infasurf (calfactant) (35 mg/ml concentration, ONY Inc, NY) was chosen for the current experiment as LS. It is a lavage of natural calf lung surfactant with no tissues which is used clinically for RDS treatment. The mixture of DPBS and 0.02 vol% of the fluorescent particle was set as the standard 'DPBS solution' for the series of experiments. 0.01 mg/ml of Infasurf was added to make 'Infasurf solution' for the current experiments. The concentration 0.01 mg/ml of Infasurf is very low in comparison with previously reported values (Glindmeyer et al. 2011). However it was a sufficient concentration to observe the surface deformation under influence of LS in the current application. It was also convenient to use the lowest concentration for the system evaluation in order to avoid the unwanted external noise factors, such as, colloidal stability and the wall contamination issues. The Infasurf solution had to be kept at 37C before and during the experiment in order for LS to work properly. It was also necessary to use it within two to three days after opening original Infasurf bottle.

Colloidal stability of the fluorescent particle is critical to ensure the quality of μ-PIV data. For investigations of airway reopening phenomena, it is necessary to use specific electrolytes, organic compounds, and proteins in order to evaluate LS functions during the measurements. The functional properties of the fluorescent particle are highly sensitive to the balance of electrical charge between the particle surface and the buffer solution.

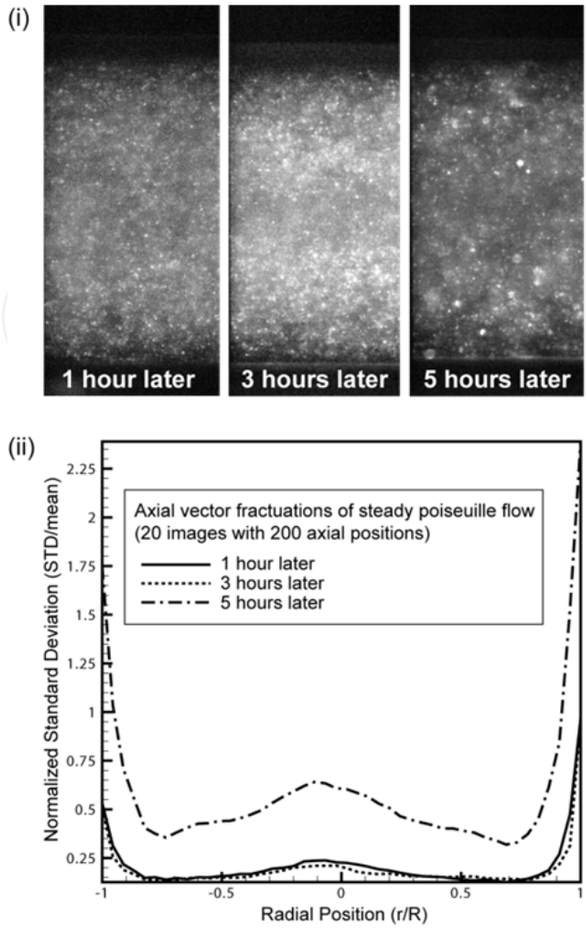

Fig. 5. Colloidal stability tests of 1.0 mg/ml Infasurf solution with 5.0 mg/ml albumin. (i) μ-PIV images of fluorescent particle flocculation at1, 3, and 5 hours. (ii) Velocity fluctuations along the channel radial direction over 100 axial positions during steady Poiseuille flow (U=5.5 mm/sec) in the cylindrical channel. After 5 hours, the particle aggregations are visible in the fluorescent images and affect on the vector interrogation result.

Even though it is safe to assume that fluorescent particles in the standard PBS are stable, since the pH of DPBS is 7.1±0.1 and the surface of the particle is cationic (Invitrogen 2004), colloidal stability under influence of Infasurf and additional LS inhibitors, such as albumin, must be carefully evaluated prior to the design of the experimental process. In order to verify the colloidal stability of the particle solution, the accuracy of μ-PIV data with a solution of 1.0 mg/ml of Infasurf with 5.0 mg/ml albumin using steady Poiseuille flow was evaluated. The capillary was filled with the solution and kept at 37C. As soon as the system reached stable temperature, the linear motor system was set to give a constant forward mean velocity at U=5.5 mm/sec , and 20 μ-PIV images were recorded. The process was repeated every 30 minutes for 5 hours. The velocity fluctuations of the ensemble axial velocity component over 100 axial positions were computed for the reliability evaluation of the vector interrogation over the progressing particle flocculation (Fig. 5). The result shows that the solution was stable for the μ-PIV data acquisition at least 3 hours after it was mixed. However, after 5 hours particle flocculation was severe and clearly identifiable either by the

visual conformation of the image or the quality of vector interrogation near the centerline. It should be noted that the experiment was design to 'boost' particle flocculation effect by adding excess amount of Infasurf and albumin. In fact, the effect of the flocculation could not be identified for the current 0.01 mg/ml Infasurf solution even after 50 hours.

2.5 Experimental procedure and data processing

The data acquisition frame rate was set to 7.5 images/sec (15 pulses/sec for the Nd:YAG laser, since the μ-PIV requires 2 frames to obtains one vector field.), and the duration of a single continuous trial was set to 60 images/run. This requires a minimum of 60/7.5=8 seconds of continuous data acquisition. Since the bubble mean velocity was defined to be 5.5 mm/sec and the translating stage provided about 10-12 cm of continuous observation window, this setting gave enough safety margin for pre- and post- adjustment time for the flow generating system.

The pulsatile frequency was Ω=2 Hz, therefore each experimental run could capture 16 cycles with 3.75 images/cycle. Repeating data acquisition and cycle averaging were employed to increase the temporal resolution (the number of image capturing points per cycle) and accuracy of ensemble averages (total number of images at the same instantaneous flow condition) to fully analyze the effect of LS on flow patterns. The stability of the testing solution shown in the previous section ensures repeatability of experimental trials. By initiating each trial with a different cycle phase, the temporal resolution was increased by accumulating the images from each repeating trial. Cycle averaging over the same experimental run was also applicable to the current application to increase the temporal resolution. Pulsating bubble surfactometer experiments have shown that cycle-averaged surface tension and the hysteresis loops of Infasurf solution were saturated after 3-4 cycles and became independent of the number of cycles (Krueger and Gaver III 2000). Therefore, the data acquisition was started after the solution passed at least ten cycles. Since the frame timing returned to the same point in the cycle every 15 image acquisition (every 4 seconds, or 4 cycles) a single continuous acquisition with cycle averaging provided 15 images/cycle with 4 images for each time-point in the cycle. In the current experimental setup, the oscillation amplitude was A=2 mm, which is wider than the microscope's field of view. Since at least 550 μm of the liquid phase ahead of the bubble tip was necessary to obtain the instantaneous downstream velocity for each image, in order to compute ensemble average, it was necessary to maintain the bubble at least 1000 μm from end of the image. Therefore at least two acquisitions focusing on different part of the cycle were necessary to capture the entire cycle with sufficient liquid phase visible in the field of view.

The simultaneous μ-PIV/shadowgraph data acquisitions for the previously described pulsatile flow condition were preformed approximately 20 times (total 1200 images) for the DPBS and the Infasurf solutions. Roughly 30% of the images were selected for analysis because they had a sufficient length of liquid phase to compute the downstream mean velocity. There images were then interrogated and filtered by using the bubble tip and channel wall geometrical information from the corresponding simultaneous shadowgraph images. The interrogation employs a recursive Nyquist grid with a FFT correlation engine and a Gaussian peak algorithm with a 64x64 pixels first interrogation window, and a 32x32 pixel second interrogation window. The resulting vector fields were validated by standard deviation, local magnitude difference, and velocity range filters. Finally, the vector fields

were divided into 16 bins based on the instantaneous downstream velocity to compute the ensemble average of each point in the cycle.

3. Results and conclusions

3.1 Image quality and efficiency of the system

Examples of the simultaneously acquired instantaneous μ-PIV and shadowgraphy images are presented in Fig. 6. In this figure Camera A provides one of the two fluorescent particle

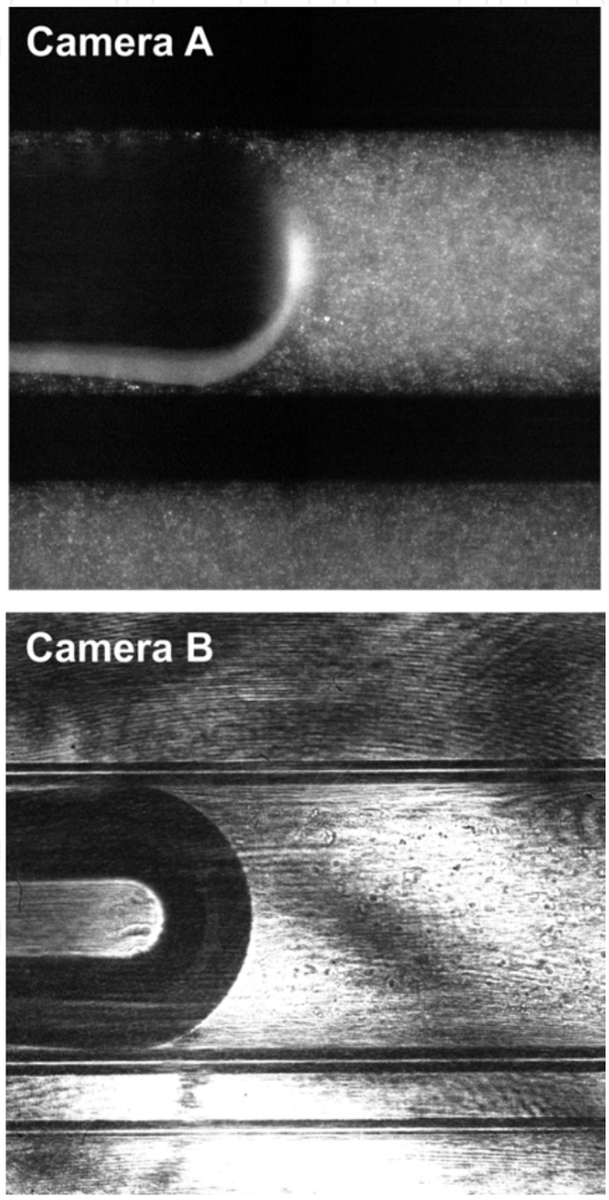

Fig. 6. Sample of simultaneously acquired μ-PIV (Camera A) and shadowgraph (Camera B) images under pulsatile flow input. Testing solution is the DPBS, and instantaneous downstream velocity is U=5.5 mm/sec.

images at an instantaneous downstream velocity U=5.5 mm/sec with the bubble progressing from left to right. U was calculated by taking the average velocity more than 1.5R downstream from the tip of the bubble. A band of fluorescent particles is visible in the lower part of image, which provides the stage velocity throughout the use of a second channel filled with the quiescent fluid. The figure demonstrates that the image separation through the dichroic filter is very good since there is virtually no cross-talk signal from the shadowgraph illumination in the particle image, and particles at the center of the channel are clearly distinguishable. As mentioned in the previous section the interfacial shape especially near the center of the channel is difficult to obtain from the fluorescent image which necessitates the use of a separate simultaneous technique to determine the interface shape.

Camera B in Fig. 6 presents the corresponding shadowgraph image. In this image, a large amount of random speckle pattern noise caused by coherent laser is visible. However, the degree of noise does not cause difficulty in determining the interfacial shape in the current case. The speckle could be eliminated by using diverse polarizations and wavelengths if necessary in future application. There is slight amount of cross-talk noise from the fluorescent particle emission due to the broad emission spectrum and less strict clean-up filter setting. This does not cause problems in the interface detection.

The interface geometry and channel wall information from Camera B were used to generate a grid mask for the vector interrogation of the Camera A image. The mask greatly increases the accuracy of the flow field measurement near the bubble tip especially during the reverse flow phase where significant interface deformations and instabilities exist. Two examples at the instantaneous downstream velocity U=-6.5 mm/sec (the bubble is progressing to the left) are shown in Fig.7. In both cases, the bubble shape estimation and the vector interrogation near the interface would be very inaccurate without the geometrical information from the corresponding shadowgraph image. Moreover, statistical analysis of the instability during the reverse flow phase is possible with this technology. This may provide information related to important physical characteristic of dynamic behavior of LS with and without competitive adsorption by using one-by-one corresponding interface shape information, flow patterns near the bubble tip and downstream velocity.

3.2 Data analysis of the bubble shape and the flow field surrounding semi-infinite bubble tip under influence of the pulmonary surfactant

The cycle averaged downstream velocities and bubble tip curvatures are displayed in Fig. 8. The data in Fig. 8-i clearly demonstrate excellent controllability of the flow generating system and the translating stage. The observed mean forward velocity is 5.5 mm/sec and the peak forward/backward velocities are about 18.5/-12.5 mm/sec. The reverse flow phase exists between $0.58< t/T < 0.92$, where T=0.5 sec is period and t is time in the sinusoidal cycle. Both the DPBS and Infasurf solutions follow the input very closely with exception of slight phase delay on the Infasurf solution due to the large interface deformation. The corresponding ensemble-averaged interfacial curvatures of the bubble tip and fluctuations at each phase are shown in Fig. 8-ii. The interfacial curvature (κ) was calculated by first applying cubic smoothing splines on the interface and computing the arc length (s) around the centerline to obtain the radius of the oscillating interface at the centreline (Ro) (Thieman 2011). Details of the interfacial curvature and flow patterns (streamlines) at the reverse flow phase with and without the effect of Infasurf are shown in Fig. 9. These figures represent the ensemble-average of over 20 instantaneous images taken at point (b) in Fig. 8-i.

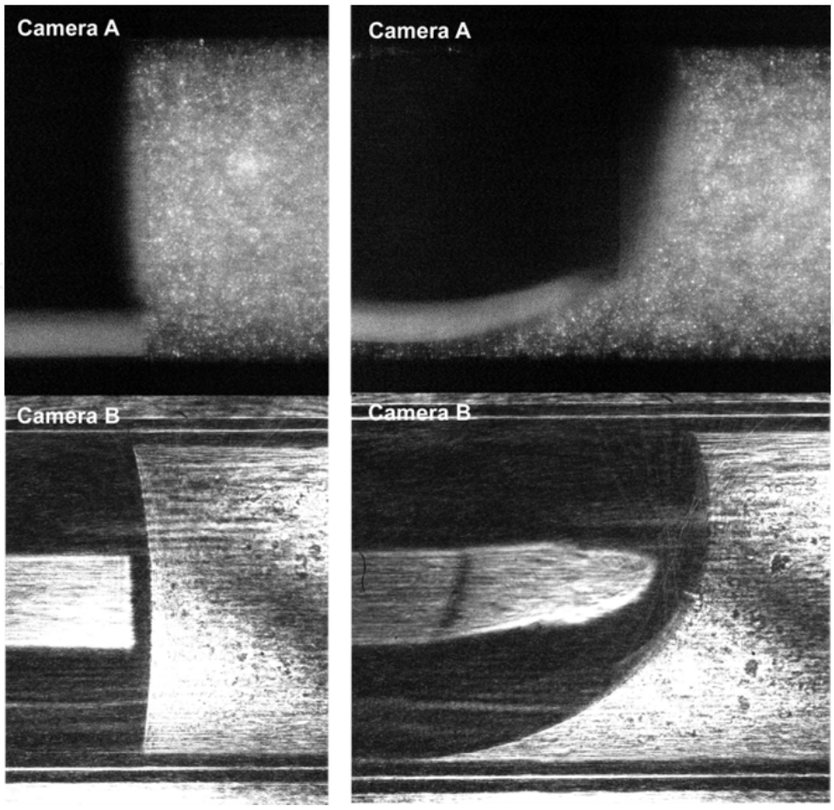

Fig. 7. Examples of the unsteady air-liquid interface during the reverse flow phase of downstream flow in pulsatile flow. The instantaneous downstream mean velocity was about U=-6.5 mm/sec for the both cases (position (b) in Fig. 8-i).

Significant interfacial deformation is only visible with the Infasurf solution during pulsatile flow. Almost negligible interface deformation is visible for the DPBS solution under the same pulsatile flow condition. The Infasurf solution with steady flow (U=5.5 mm/sec, gray straight line with circle in Fig. 8-ii) does not show any deformation. This experimental result is consistent with the hypothesis presented in Fig. 2 that predicts a significant interfacial deformation for the Infasurf solution during pulsatile flow.

During the reverse flow phase, converging stagnation region (ring in 3D) is located near the capillary walls (Fig. 9). Since the multi-layer formation and collapse of Infasurf dramatically lower the local surface tension relative to the expanding (diverging) region at the center (Fig. 2-i), the gradient of surface tension causes strong Marangoni stress tangential to the interface and rigidifies the interface. The very small curvature shift of the DPBS solution suggests insignificance of fluid dynamic effect on the interface shape. The curvature of the Infasurf solution during the forward flow phase is constantly lower than exists with steady flow due to the consistently lower surface tension caused by larger surface accumulation of Infasurf throughout the pulsatile motion. Glindmeyer et al. (2011) recently performed in-vitro experiments of LS effects on cell-laden rigid tube, and reported reduced cell damage during the reverse flow region. This finding coincides with the change of the interface and flow pattern near the bubble tip, and provides a physicochemical basis for the reduction of cell damage.

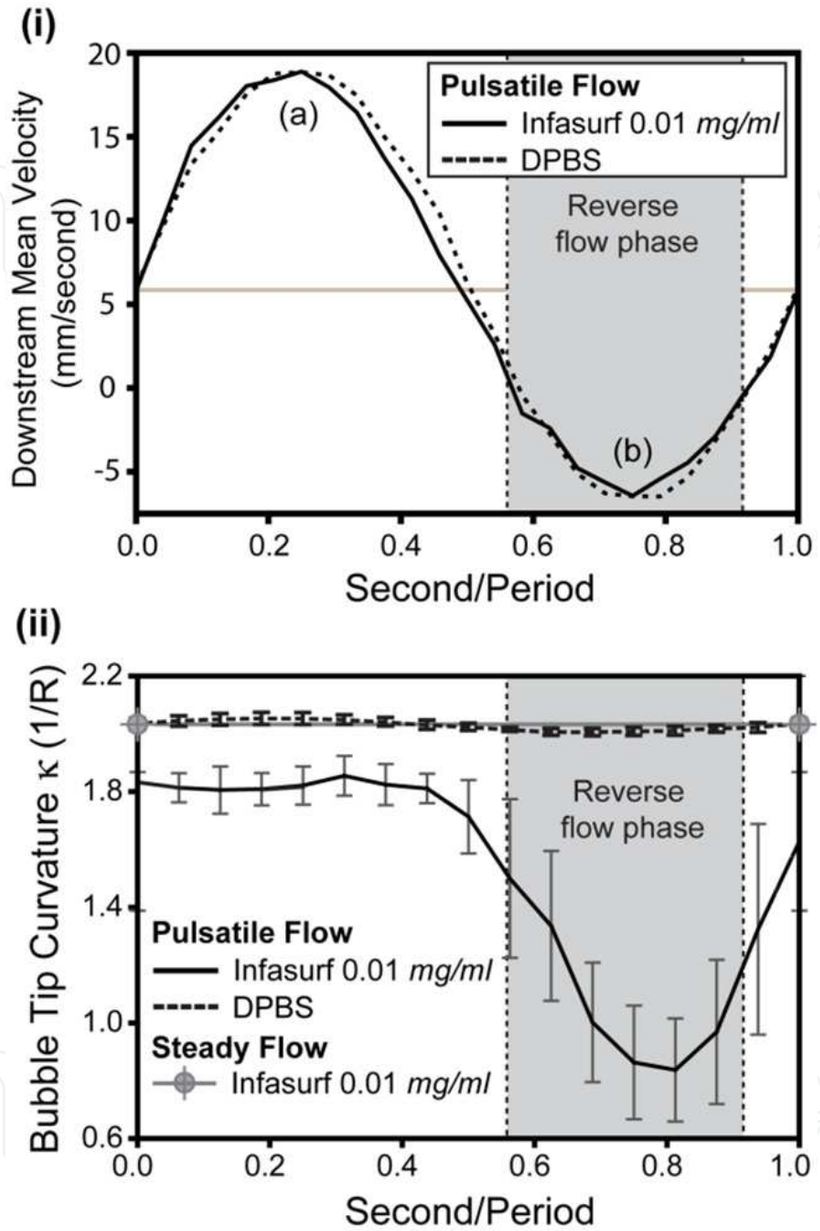

Fig. 8. (i) Measured downstream mean velocity in the cycle, and (ii) corresponding bubble tip curvature. Only the Infasurf solution display significant bubble interface deformation and fluctuation of curvature (see Fig. 7) during the reverse flow phase. The result is explained very well by the LS adsorption/desorption prediction model (Fig. 2), since the DPBS under the same flow condition and the Infasurf without sinusoidal flow input do not show similar deformations.

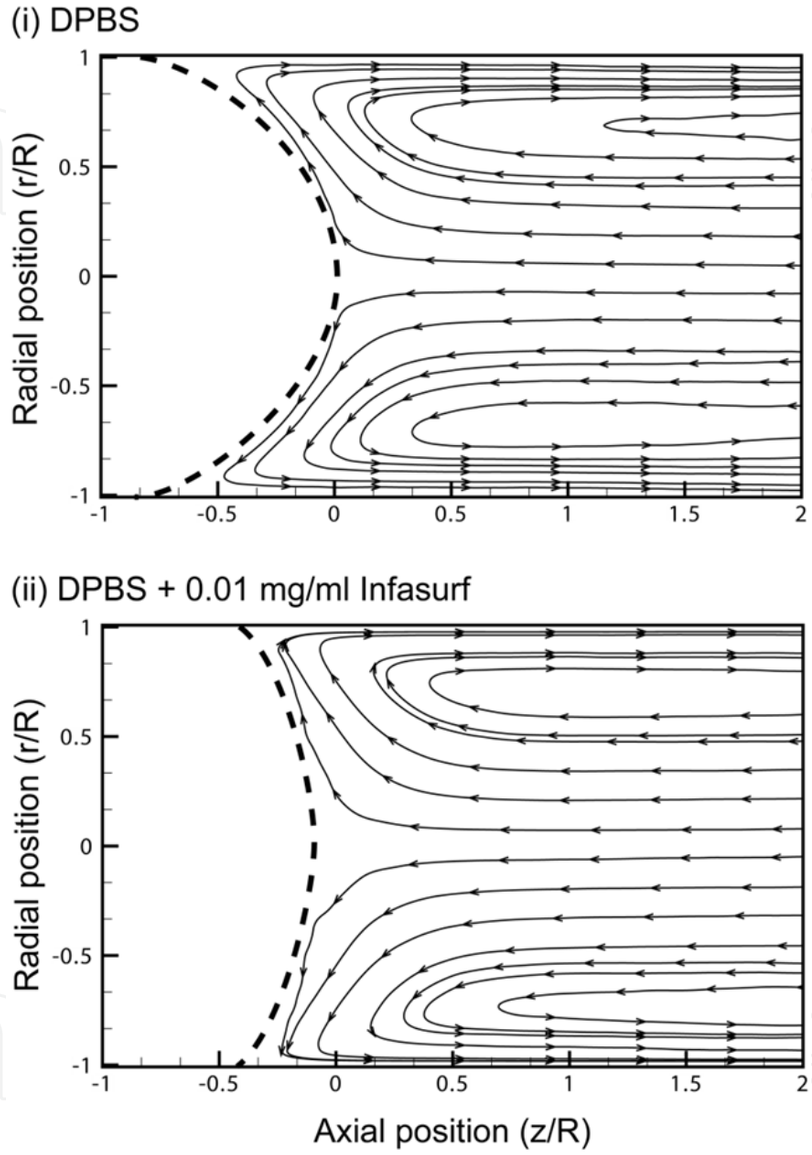

Fig. 9. Ensemble averaged streamlines and bubble shapes. Both figures have the same downstream mean velocity U=5.9 mm/sec (position (b) in Fig. 8-i). The bubble shape and flow pattern in (II) are significantly altered by accumulated LS around converging stagnation points (ring in 3D) near the wall. This difference has been observed only during the reverse flow region, and matches very well with reduced cellular damage that exists during reverse flow observed of in-vitro experiments (Glindmeyer et al. 2011).

An increasing curvature fluctuation (instability) is also noticeable during the reverse flow phase with the pulsatile flow and Infasurf (examples of unsteady interface are shown in Fig. 7). It can be hypothesized that the increasing fluctuation is a result of weakened wetting of the contaminated glass capillary wall since a glass surface is hydrophilic and has almost perfect wettability. Therefore if any kind of protein substances from the Infasurf solution adheres to the surface, it will certainly cause a loss of wettability. Since the trailing edge of tip of the semi-infinite bubble is a thin-film region, surface stability which is sensitive to surface energy balance is very low at the contaminated area causing dewetting regions. This is not a problem for a forwarding bubble, because the thin-film region is behind it. However, for the reverse flow the region is traversed by the returning bubble interface during a stage when it has the lowest local surface tension point very close to the wall. A re-wetting of the relatively hydrophobic region certainly causes stiff 'stick-slip' motions of the interface near the wall and results in widely diverged unevenly deformed instantaneous interface shapes during the reverse flow phase.

The simultaneous acquisition allows researchers to examine every single instantaneous velocity profile with a corresponding interfacial shape. Therefore vector fields of obviously skewed bubble tip shapes could be eliminated manually during the process of ensemble averaging, if they want to focus on LS effect and subsurface flow pattern. This will be increasingly important for the analysis of multi-phase fluid dynamics regarding the airway reopening problem, since obvious further investigations of the current application are to examine effects of higher Infasurf concentration to interface shape and interactions between LS inhibitors. It is possible to approach the contamination of the glass tube by developing a surface modification technique for the glass surface. For example, protein contaminations can be reduced by using a surface coating agent such as 2-[methoxy(polyethylenxy-propyl)trimethoxysilane (Tech-90, Gelest Inc., PA). This grafts poly(ethylene glycol) polymer chains on glass surface (Sui et al. 2006) and reduces nonspecific binding of proteins in the Infasurf solution. Using the simultaneous μ-PIV/shadowgraph acquisition system will also be a powerful tool to examine the effectiveness of various surface modification methods by evaluating the fluctuations during the reverse flow phase.

In summary, the simultaneous μ-PIV/shadowgraph acquisition system has been demonstrated as a powerful analysis tool for the complex multi-phase micro-biofluidic investigation, such as investigation of physicochemical interaction of lung surfactant during mechanically ventilated reopening of fluid-occluded respiratory airway. Complex flow controls, continuous data acquisition, and the simultaneous μ-PIV/shadowgraph acquisition with two separate cameras are all required to investigate this system, and the successful combination of the system opens the door to further investigations of this complex system and will allow the investigation of the role of LS inhibitors and the effect of surface properties to the flow fields.

4. Acknowledgment

This material is based upon work supported by the National Science Foundation under grant No. CBET-1033619, and the National Institutes of Health through grant R01-HL81266

5. References

Adrian, R. J. (2005). Twenty years of particle image velocimetry. *Experiments in Fluids*, Vol.39. pp.159-169.

Bilek, A. M., Dee, K. C. and Gaver III, D. P. (2003). Mechanisms of surface-tension-induced epithelial cell damage in a model of pulmonary airway reopening. *Journal of Applied Physiology*, Vol.94. pp.770-783.

Clements, J. A. and Avery, M. E. (1998). Lung surfactant and neonatal respiratory distress syndrome. *American Journal of Respiratory ad Critical Care Medicine*, Vol.157. pp.S55-S66.

Fairbrother, F. and Stubbs, A. E. (1935). Studies in electro-endosmosis VI. The bubble tube method of measurement. *Journal of Chemical Society*, Vol.1. pp.527-529.

Gaver III, D. P., Halpern, D., E., J. O. and Grotberg, J. B. (1996). The steady motion of a semi-infinite bubble through a flexible-walled channel. *Journal of Fluid Mechanics*, Vol.319. pp.25-65.

Gaver III, D. P., Jacob, A.-M., Bilek, A. M. and Dee, K. C. (2006). The significance of air-liquid interfacial stresses on low-volume ventilator-induced lung injury, *Ventilator-induced lung injury*, Dreyfuss, D., Saumon, G. and Hubmayr, R. D., New York, Taylor & Francis Group, Vol.215, pp.157-203.

Gaver III, D. P., Samsel, R. W. and Solway, J. (1990). Effects of surface tension and viscosity on airway reopening. *Journal of Applied Physiology*, Vol.69. pp.74-85.

Glindmeyer, H. W. I., Smith, B. J. and Gaver III, D. P. (2011). In Situ enhancement of pulmonary surfactant function using temporary flow reversal. *Journal of Applied Physiology*, Vol. (accepted).

Huh, D., Fujioka, H., Tung, Y.-C., Futai, N., Paine III, R. and Grotberg, J. B. (2007). Acoustically detectable cellular-level lung injury induced by fluid mechanical stress in microfluidic airway systems. *Proceedings of the National Academy of Science*, Vol.104, No.48. pp.18886-18891.

Invitrogen (2004), Propaties and Modifications, *Working with FluoSpheres fluorescent microspheres*: Vol.

Jacob, A.-M. and Gaver III, D. P. (2005). An investigation of the influence of cell topography on epithelial mechanical stresses during pulmonary airway reopening. *Physics of Fluids*, Vol.17. pp.031502.

Kay, S. S., Bilek, A. M., Dee, K. C. and Gaver III, D. P. (2004). Pressure gradient, not exposure duration, determines the extent of epithelial cell damage in a model of pulmonary reopening. *Journal of Applied Physiology*, Vol.97. pp.269-276.

Krueger, M. A. and Gaver III, D. P. (2000). A theoretical model of pulmonary surfactant multilayer collapse under oscillating area conditions. *Journal of Colloidal and Interface Science*, Vol.229. pp.353-364.

Mclntyre, R. C., Pulido, E. J., Bensard, D. D., Shames, B. D. and Abraham, E. (2000). Thirty years of clinical trials in acute respiratory distress syndrome. *Critical Care Medicine*, No.28. pp.9.

Meinhart, C. D., Wereley, S. T. and Santiago, J. G. (1999). PIV measurements of a microchannel flow. *Experiments in Fluids*, Vol.27. pp.414-419.

Meinhart, C. D., Wereley, S. T. and Santiago, J. G. (2000). A PIV algorithm for estimating time-averaged velocity fields. *Journal of Fluid Engineering*, Vol.122. pp.285-289.

Mielink, M. M. and Saetran, L. R. (2006). Selective seeding for micro-PIV. *Experiments in Fluids*, Vol.41. pp.155-159.

Natrajan, V. K., Yamaguchi, E. and Christensen, K. C. (2007). Statistical and structural similarities between micro- and macroscale wall turbulence. *Microfluid Nanofluid*, Vol.3. pp.89-100.

Nogueira, S., Sousa, R. G., Pinto, A. M. F. R., Riethmuller, M. L. and Campos, J. B. L. M. (2003). Simultaneous PIV and pulsed shadow technique in slug flow: a solution for optical problems. *Experiments in Fluids*, Vol.35. pp.598-609.

Olsen, M. G. and Adrian, R. J. (2000). Out-of-focus effects on particle image visibility and correlation in microscopic particle image velocimetry. *Experiments in Fluids*, Vol.Suppl. pp.S166-S174.

Pillert, J. E. and Gaver III, D. P. (2009). Physicochemical Effects Enhance Surfactant Transport in Pulsatile Motion of a Semi-Infinite Bubble. *Biophysical Journal*, Vol.96, No.1. pp.312-327.

Santiago, J. G., Wereley, S. T., Meinhart, C. D., Beebe, D. J. and Adrian, R. J. (1998). A Particle image velocimetry system for microfluidics. *Experiments in Fluids*, Vol.25. pp.316-319.

Smith, B. J. and Gaver III, D. P. (2008). The pulsatile propagation of a finger of air within a fluid-occluded cylindrical tube. *Journal of Fluid Mechanics*, Vol.601. pp.1-23.

Smith, B. J., Lukens, S., Yamaguchi, E. and Gaver III, D. P. (2011). Lagrangian transport properties of pulmonary interfacial flows. *Journal of Fluid Mechanics*, Vol.Accepted.

Smith, B. J., Yamaguchi, E. and Gaver III, D. P. (2010). A translating stage system for μ-PIV measurements surrounding the tip of a migrating semi-infinite bubble. *Measurement Sicence and Technology*, Vol.21, No.1. pp.15401-15413.

Sui, G., Wang, J., Lee, C.-C., Lu, W., Lee, S. P., Leyton, J. V., Wu, A. M. and Tseng, H.-R. (2006). Solution-phase surface modification in intect Poly(dimethylsiloxane) microfluidic channels. *Analytical Chamistry*, Vol.78, No.15. pp.5543-5551.

Thieman, J. W. (2011). The development of digital signal processing techniques to estimate stress fields in biological two-phase flows. The Department of Biomedical Engineering. New Orleans, Tulane University. Master of Science.

Ware, L. B. and Matthay, M. A. (2000). The acute respiratory distress syndrome. *The New England Journal of Medicine*, Vol.342, No.18. pp.1334-1349.

Yalcin, H. C., Perry, S. F. and Ghadiali, S. N. (2007). Influence of airway diameter and cell confluence on epithelial cell injury in an in vitro model of airway reopening. *Journal of Applied Physiology*, Vol.103. pp.1796-1807.

Yamaguchi, E., Smith, B. J. and Gaver III, D. P. (2009). μ-PIV measurements of the ensemble flow fields surrounding a migrating semi-infinite bubble. *Experiments in Fluids*, Vol.47, No.2. pp.309-320.

Zasadzinski, J. A., Stenger, P. C., Shieh, I. and Dhar, P. (2010). Overcoming rapid inactivation of lung surfactant: Analogies between competitive adsorption and colloid stability. *Biochimica et Biophysica Acta*, Vol.1798. pp.801-828.

Zimmer, M. E., Williams, H. A. R. and Gaver III, D. P. (2005). The pulsatile motion of a semi-infinite bubble in a channel: flow fields, and transport of an inactive surface-associated contaminant. *Journal of Fluid Mechanics*, Vol.537. pp.1-33.

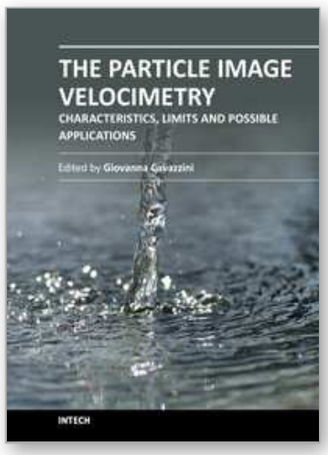

The Particle Image Velocimetry - Characteristics, Limits and Possible Applications

Edited by PhD. Giovanna Cavazzini

ISBN 978-953-51-0625-8
Hard cover, 386 pages
Publisher InTech
Published online 23, May, 2012
Published in print edition May, 2012

The Particle Image Velocimetry is undoubtedly one of the most important technique in Fluid-dynamics since it allows to obtain a direct and instantaneous visualization of the flow field in a non-intrusive way. This innovative technique spreads in a wide number of research fields, from aerodynamics to medicine, from biology to turbulence researches, from aerodynamics to combustion processes. The book is aimed at presenting the PIV technique and its wide range of possible applications so as to provide a reference for researchers who intended to exploit this innovative technique in their research fields. Several aspects and possible problems in the analysis of large- and micro-scale turbulent phenomena, two-phase flows and polymer melts, combustion processes and turbo-machinery flow fields, internal waves and river/ocean flows were considered.

INTECH
open science | open minds

InTech Europe
University Campus STeP Ri
Slavka Krautzeka 83/A
51000 Rijeka, Croatia
Phone: +385 (51) 770 447
Fax: +385 (51) 686 166
www.intechopen.com

InTech China
Unit 405, Office Block, Hotel Equatorial Shanghai
No.65, Yan An Road (West), Shanghai, 200040, China
中国上海市延安西路65号上海国际贵都大饭店办公楼405单元
Phone: +86-21-62489820
Fax: +86-21-62489821

IntechOpen